Contents lists available at ScienceDirect

Coastal Engineering

Experimental reproduction of inhomogeneous fjord waves

Sébastien Laflèche [a,b,*], Konstantinos Christakos [b,c], Babak Ommani [b], Sébastien Fouques [a], Trygve Kristiansen [b]

[a] *SINTEF Ocean, Trondheim, 7050, Norway*
[b] *Department of Marine Technology, NTNU, Jonsvannsveien 82, Trondheim, 7050, Norway*
[c] *Norwegian Meteorological Institute, Bergen, Norway*

ARTICLE INFO

ABSTRACT

Waves in coastal areas and fjords can present inhomogeneities that affect the responses of very large floating structures. However, spatial inhomogeneities of waves are usually not included in model testing. In this paper, the feasibility of generating inhomogeneous wave conditions in an Ocean basin is investigated. For that purpose, a fast linear numerical model of a basin of constant depth is applied, and an optimization method is presented, that allows to find the control signal for the multiflap wavemaker. Comparisons with experiments in SINTEF's Ocean basin demonstrate the validity of the method for generating simple monochromatic synthetic waves, as well as short-crested irregular waves representing realistic conditions in Sulafjorden.

1. Introduction

In coastal areas, and especially in fjords (deep, long and narrow inlets of water), complex topography leads to wave conditions unlike those observed offshore. In particular, waves in coastal areas and fjords can be inhomogeneous, which means that wave statistics can change rapidly spatially. In Gaussian linear wave theory, this simply means that the directional spectrum varies in space. In recent years, wave inhomogeneities have begun to be the focus of several projects related to the documentation of wave conditions in the Norwegian fjords and coastal areas (Cheng et al., 2019; Stefanakos et al., 2021; Christakos et al., 2022).

The motivation for those studies was mainly the Norwegian coastal highway route E39 project (Dunham, 2016). This project, carried out by the Norwegian Public Roads Administration, includes the construction of long suspension bridges, floating bridges, or submerged floating tunnels for several fjord crossings. For floating bridges of large scale, responses are sensitive to inhomogeneous wave load effects, so that the latter needs to be taken into account in the design phase (Cheng et al., 2018; Dai et al., 2021). Sensitivity to inhomogeneities is also a question for other large-scale floating structures (Wei et al., 2017; Yang et al., 2019), or array of floating structures.

The Large Floating Coastal Structures project report by Abrahamsen and Stansberg (2019) provides an extensive literature study on model testing of large structures. However, as they point out, up to now, spatial inhomogeneities are not usually included in model testing,

except when reproducing the actual bathymetry in coastal basins. New methods to experimentally generate inhomogeneous environments need then to be developed for Ocean basins. Rodrigues et al. (2022) carried out model tests of a floating bridge with inhomogeneous waves. But even so, this was done simply by having the amplitude of the motion of the flaps vary linearly with their position along the length of the wavemaker, without further control of the wave field in the basin. Two main challenges can thus be identified. First, describing wave conditions in fjords or coastal areas to know which target wave one should aim to reproduce in hydrodynamic laboratories. Then, designing methods to reproduce a given inhomogeneous wave in a basin. The focus of the article is this second challenge.

Several authors have discussed the theory of wave generation and propagation in a wave tank. It was first derived within the assumption of two-dimensional wave propagation by Biésel and Suquet (1951) within the assumption of linear wave theory, and extended to second order by Schäffer (1996). The theory was then extended to also include homogeneous short-crested waves, both at first and second order by Schäffer and Steenberg (2003). The question of inhomogeneous waves first became a topic as an unwanted phenomenon to mitigate. When performing tests with homogeneous waves, Takayama (1984) and Gilbert and Huntington (1991) among others noticed that without special care, the generated waves in an Ocean basin were not perfectly homogeneous. Various techniques were then designed to both predict the inhomogeneities of the wave field and to enlarge the working area

---

in Ocean basins with simple geometries (Dalrymple, 1989; Molin, 1991; Matsumoto and Hanzawa, 1996) or more complex ones (Ota et al., 2021; Laflèche et al., 2023). However, for all those cases, inhomogeneities are an unwanted phenomenon, and the target wave field is homogeneous.

When the target wave field is homogeneous, it is often specified as a realization of a given directional spectrum. However, this wave-generation process cannot directly be applied to inhomogeneous sea states. Indeed, drawing random phases from a directional spectrum implies assuming homogeneity. Thus, without phase information, a single directional spectrum can only be used to describe homogeneous wave conditions.

This paper investigates the feasibility of generating realistic inhomogeneous conditions in an Ocean basin. It adapts the methodology used for modelling and control of the basin presented in Laflèche et al. (2023) for improving the homogeneity of waves in a basin of constant depth, but this time aiming at the reproduction of a target inhomogeneous wave field. Following the recent interest in building floating bridges, we focus on fjord waves, i.e., waves in sheltered or semi-sheltered coastal areas with deep water. Laboratory experiments were conducted in the Ocean basin at SINTEF Ocean in order to test the validity of the method. Two test cases were chosen. The first one is the reproduction of an arbitrary synthetic wave: a regular wave, but with an amplitude following a step function in the transverse direction with respect to wave propagation. The other one corresponds to realistic wave conditions in two different sites in Sulafjorden, which is fjord semi-exposed to the open ocean. To that purpose, a target wave field was obtained using the phase-resolving fully non-linear potential flow solver REEF3D::FNPF (Wang et al., 2023).

The paper is divided as follows. The first part presents the process developed to generate a specified inhomogeneous wave field in an Ocean basin. The presentation of the experimental setup follows, and the method is illustrated with an arbitrary synthetic target wave. The test cases corresponding to realistic fjord waves are then presented, as well as the technique used to obtain the target wave. The results of the experimental campaign are presented and discussed subsequently. Finally, the generalization of the method is discussed.

2. Method

2.1. Formulation of the numerical problem

The problem here is to reproduce given time series of free-surface elevation $\zeta(x, y, t)$ in a given area of a three-dimensional wave basin. The coordinate system is taken so that z is positive upwards. Those time series define a target wave field which is, in the general case, irregular, short-crested, and inhomogeneous.

Waves in the basin are generated by a multiflap wavemaker with N flaps. The displacement of a flap is $X_n(z, t)$, where $n \in [\![1, N]\!]$. The goal is then to find the optimal time series for all $X_n(z, t)$ for which the generated waves are the closest possible to the target wave.

In the following, potential flow theory is assumed, and the waves are assumed to be of small steepness, so that linear wave theory can be used. In addition, constant water depth is also assumed. Those are reasonable assumptions for waves in fjords, as they are usually deep and sheltered. Indeed, even if variations in bathymetry cannot be neglected in coastal areas when simulating wave propagation from offshore areas, they can however be negligible locally around a structure. If they are negligible in the domain of interest reproduced in the basin, then a basin with constant water depth can be used. The validity of those assumptions for the case of Sulafjorden is discussed in Section 5.1.5.

2.2. Numerical wave tank

A panel method is applied to describe the waves generated by a multiflap wavemaker. It is this panel method that is referred to as

numerical wave tank in the present article. The method is described in Laflèche et al. (2023). It assumes a constant water depth h. Thus, the vertical dependency can be solved analytically and the problem to be solved becomes two-dimensional only. As the model is linear, it solves for the free-surface elevation in the frequency domain. For a given angular frequency ω, let k be the real wavenumber given by the linear dispersion relationship $\omega^2 = gk \tanh(kh)$, and g be the acceleration of the gravity. The equation that is solved is then the 2D Helmholtz equation

$$\left(\Delta + k^2\right)\eta = 0 \tag{1}$$

where Δ is the 2D Laplacian with respect to (x, y), and $\eta(x, y)$ is the complex amplitude of the wave at this frequency (that is, the Fourier transform in time of $\zeta(x, y, t)$ taken at the angular frequency ω). The method then gives in frequency domain the complex amplitude of the free-surface elevation at any point in the basin, $\eta(\mathbf{X})$, as a function of the complex amplitude of the displacement of each flap, $X_{a,n}$.

The problem can be written as a boundary value problem, and solved with a panel method. As the domain is two-dimensional, its boundaries are lines, on which sources and dipoles are distributed. Sources are solutions of Eq. (1) with a radiation condition prescribed at infinity. The intensity of a source at a point $\mathbf{P}$ measured at a point $\mathbf{Q}$ is

$$G_{\mathbf{P}}(\mathbf{Q}) = -\frac{i}{4} H_0^{(1)}(kr) \tag{2}$$

where $H_0^{(1)}$ is the zeroth-order Hankel function of the first kind, and $r = \|\mathbf{Q} - \mathbf{P}\|$. Because of the radiation condition, perfectly absorbing boundaries can be modelled as openings into an infinite domain. At the wavemaker, the displacement of the flap gives the intensity of the source distribution. For all the other sources and dipoles, the boundary conditions give a linear system of equations to be solved. It should be noted that for a perfectly reflecting wall, only dipoles are used. Alternatively, a symmetry condition can also be used to describe a perfectly reflecting wall on a side of the domain. It can also be used for the wall on which the wavemaker is if the wavemaker does not have active absorption.

The dimensions of the Ocean basin that was modelled in the present work are presented in Fig. 1. The beaches (BM2- and BM3-beach) were modelled as openings into an infinite domain. All walls were supposed to be perfectly reflecting, and a symmetry condition was used both at $x = 0$ m and at $y = 0$ m. The other walls were modelled as a distribution of dipoles.

2.3. Optimization method

The numerical wave tank gives the transfer function $\eta_n(\mathbf{X})$ between the complex amplitude of the displacement of each wavemaker flap and the free-surface elevation at any point in the basin, as a function of frequency. The optimization problem is then to find the time series for the movement of each flap, that generates waves that are as close as possible to the target waves in an area of interest. In frequency domain, this means finding the complex amplitude $X_{a,n}$ of the wavemaker motion for each flap.

The method used is taken directly from Laflèche et al. (2023). The optimization is performed in frequency domain, using the linearity of the equations. The following steps are performed for each frequency component,

1. We choose an array of points $\mathbf{X}_i$ on which we want the waves to be as close as possible to the target waves.
2. From the target wave, we retrieve the complex amplitudes $\eta_{target}(\mathbf{X}_i)$.
3. For each wave flap, we use the numerical wave tank to obtain the wave field corresponding to a unitary displacement of the flap. This gives the transfer functions $\eta_n(\mathbf{X})$.
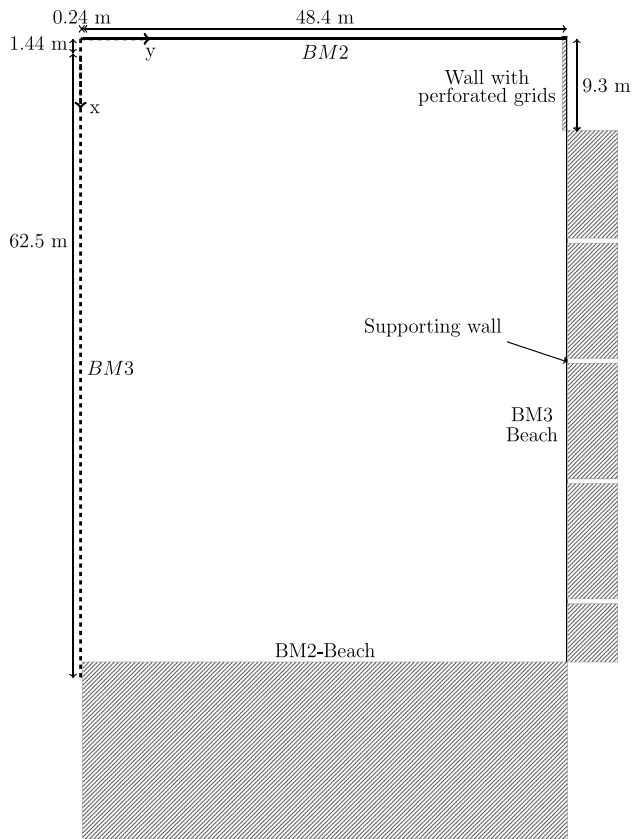
Fig. 1. Dimensions of SINTEF's Ocean basin used for the experiments — BM3 indicating the multi-flap wavemaker, and BM2 indicating another single-flap wavemaker not used in this test campaign.

Fig. 2. Position of the wave probes (black crosses) in the array — The axis are relative to the centre of the array, as the array was moved to several positions across the basin.

Table 1
Test program for the first case study: monochromatic synthetic waves — Wave period T given in model scale.

Type of inhomogeneity	T [s]	Steepness (H/λ)
Transverse step function	1.5	1/45
Transverse step function	2	1/45

Table 2
Test program for the second case study: irregular fjord waves — $\overline{H_s}$ and $\overline{T_p}$ indicate average values in the domain, and are given in model scale.

Location	$\overline{T_p}$ [s]	$\overline{H_s}$ [m]
Entrance of Sulafjorden	2.1	0.037
Inside Sulafjorden	2.2	0.011

The wave field produced by any vector of flap motion $\mathbf{X}_a = \left(X_{a,1} \cdots X_{a,N} \right)^T$ can be written as $\sum_{n=1}^{N} X_{a,n} \eta_n(\mathbf{X})$, without further use of the numerical wave tank.

4. We find the vector $\mathbf{X}_a$ that minimizes the difference between the target wave field and that obtained from the numerical wave tank.

A standard least-square method is used for the optimization. The goal function is the difference between numerical and target complex amplitudes of the free-surface elevation,

$$f(\mathbf{X}_a) = \frac{1}{M} \sum_{i=1}^{M} \left| \sum_{n=1}^{N} X_{a,n} \eta_n(\mathbf{X}_i) - \eta_{target}(\mathbf{X}_i) \right|^2 \tag{3}$$

The only unknowns are the $X_{a,n}$, and the gradient of f is straightforward to derive. Thus, a gradient-based method can be used. In the present work, the MATLAB® function *fmincon* (MATLAB, 2022), using an interior-point method, was chosen.

As the numerical wave tank used for this method takes into account the geometry of the basin, the optimization includes by construction a correction of the unwanted inhomogeneities present also when generating homogeneous waves (Laflèche et al., 2023).

3. Setup

3.1. Experimental setup

Dedicated experiments were performed in the Ocean basin at SINTEF Ocean during July 2022 (see Fig. 1). Wave measurements were performed with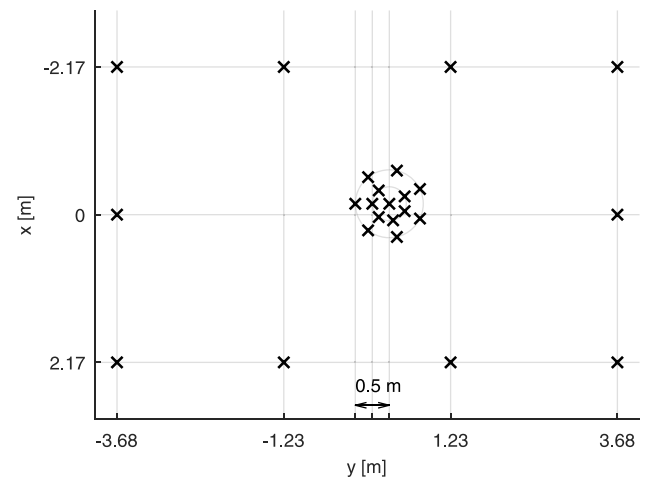 a wave probe array, composed of 10 probes on a rectangular grid with a spacing of 2.17 m by 2.45 m, around a small circular array of 14 probes, as shown in Fig. 2. Waves were generated with a multiflap wavemaker (BM3 in Fig. 1), composed of 143 flaps with a width of 0.43 m each. The water depth was 5 m. Each wave was then repeated several times, moving the wave probe arrays between each repetition, in order to map a large area of the basin. The free surface was brought to rest between tests.

Repeatability errors can occur both in the measurement and in the wave generation. In order to quantify them, a test wave, that is a specific regular long-crested wave, was repeated several times during the test campaign. Repeatability errors proved to be less than ±2%.

A summary of the test program is given in Tables 1 and 2. It is then presented in detail separately for each case study. All waves were inhomogeneous. It included two monochromatic waves at 1.5 s and 2 s for the synthetic case, and irregular waves for the fjord waves. Unless precised otherwise, all quantities are given in model scale.

3.2. Data processing

3.2.1. Correlation

Time series of free-surface elevation are obtained from the target waves, the numerical wave tank, and the experimental measurements. Comparison can be done directly by looking at the time series on a few chosen points of interest. To have an overview of differences over the whole domain, in addition to looking directly at time series, it was chosen to look at their correlation, that is, Pearson's correlation coefficient:

$$\rho_{\zeta_1,\zeta_2} = \frac{\text{cov}\left(\zeta_1, \zeta_2\right)}{\sigma_{\zeta_1} \sigma_{\zeta_2}} \tag{4}$$

where

$$\text{cov}\left(\zeta_1, \zeta_2\right) = \mathbb{E}\left[\zeta_1 \zeta_2\right]$$
$$\approx \frac{1}{t_2 - t_1} \int_{t_1}^{t_2} \zeta_1(t)\zeta_2(t)\, dt, \quad (5)$$

σ indicates standard deviation, and t_1 and t_2 are the boundaries of the time window of interest. The two time series that are compared, ζ_1 and ζ_2, are time series of free-surface elevation at one given location, but from two different datasets (for instance ζ_1 being numerical results and ζ_2 either the target wave or experimental measurements).

Correlation captures both differences in phase and amplitude, with one exception: the amplitudes of two time series that have a correlation of 1 can still differ, but only by multiplication by a constant factor. This makes correlation an irrelevant quantity for comparing amplitudes of regular waves, but still meaningful for irregular waves. It should be noted however that, as correlation captures only an average over time, it cannot capture discrepancies related to a single wave event.

3.2.2. Time window and synchronization

The time window was chosen so that waves would have the time to propagate from the wavemaker to the probes, and so that waves reflected by the beach opposing the wavemaker have not reached the probes yet. Those time instants were obtained considering propagation of each frequency component at its group velocity, assuming linear wave theory. Considering the wave periods analysed, in the whole study, the time window is between $t_1 = 45$ s and $t_2 = 80$ s, for all probes.

Synchronization of the time series was performed using signals from the flap motions of the wavemaker. For each repetition of each wave, the time lag between the measured displacement of the flaps and their control signal was computed, and then applied to all measured data of free-surface elevation.

4. Case study: Synthetic waves

4.1. Definition

The first test case is the reproduction of a synthetic target wave field, that is, arbitrarily chosen target waves. The target wave is monochromatic, propagating in the direction of increasing y, but with an amplitude that varies with x (see Figs. 4 and 5). More precisely, the amplitude $|\zeta|$ follows a step function, $|\zeta(x, y, t)| = A \times H(x_0 - x)$, where H is the Heaviside step function, and $x_0 = 35.5$ m. A is chosen so that the steepness of the wave is $2A/\lambda = 1/45$, where λ is the wavelength. Two wave periods were considered for this test case, $T = 1.5$ s and $T = 2$ s.

For each case, optimization was performed using the numerical wave tank in order to give the motion of each flap, as described in Section 2. As the target waves are monochromatic, the displacement of each flap is also monochromatic, and can be expressed as $X_n(z,t) = X_{a,n} S(z) e^{-i\omega t}$, where $S(0) = 1$. The values of $X_{a,n}$ for $T = 1.5$ s are presented in Fig. 3. From the displacement of each flap, the numerical wave tank also gives the numerical wave field. Model tests were then conducted with the wave probe array placed in two different positions, in order to capture the free-surface elevation on both sides of the step in the target ζ.

4.2. Results

Results from both the numerical model and the Ocean basin tests, for both wave periods, are provided in Fig. 4 for the wave at $T = 1.5$ s, and in Fig. 5 for the one at $T = 2$ s. Experimental data from the 20 probes and 2 circular arrays are represented by circles with colour to compare with the background colour representing the numerical results. The numerical wave tank predicts that waves cannot follow exactly the target wave. This was expected, as the target wave is not feasible, that is, not a solution of the 2D Helmholtz equation.
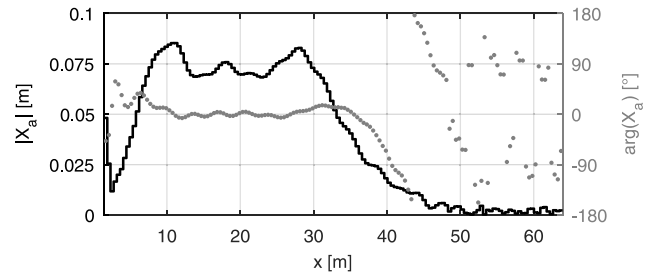

Fig. 3. Complex amplitude of the motion of each flap (at $z = 0$ m) given by the optimization process for the synthetic target wave at $T = 1.5$ s.
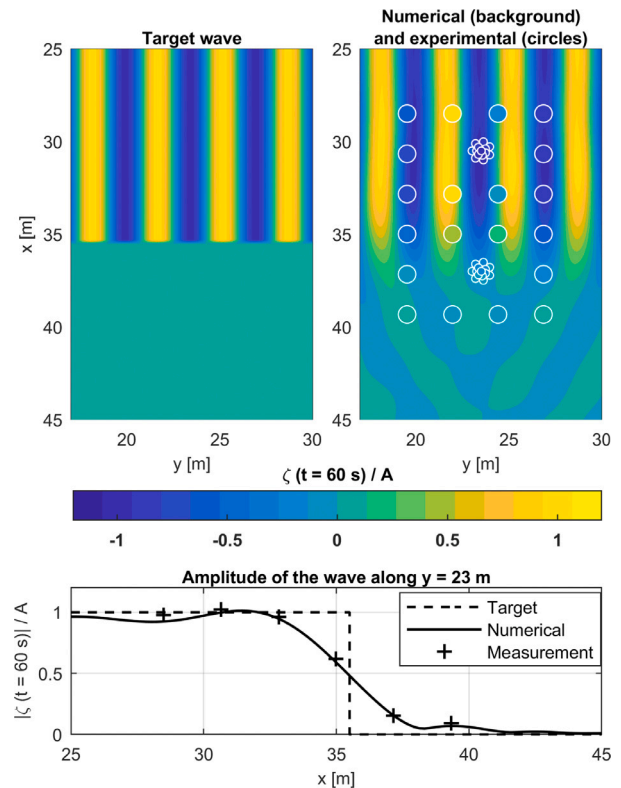

Fig. 4. Comparison of the free-surface elevation of the target wave, the numerical results and the experimental measurements (each circle represents one wave probe), for the synthetic target wave at $T = 1.5$ s, before reflection from the beach — Snapshot of free-surface elevation, and evolution of the amplitude of the waves along the transverse direction.

The numerical results for the transverse variation of the amplitude do not give a discontinuous step, but a progressive slope going from A to 0. A comparison of the length scale of the slope for both wave periods shows that the length scale of this slope is proportional to the wavelength: this can give a first estimate of the characteristic length for the amplitude variations of an inhomogeneous wave. Looking at the numerical results, for $x \geq x_0$, components of very low amplitude can be observed that travel radially from the wavemaker to the centre of the domain, and then radially outwards, towards the beach. Those components correspond to the diffraction that would happen if an obstacle was present at $x \geq x_0$, and in the centre of the domain in the y direction. It is reasonable to think that this case is indeed the closest feasible wave to the target wave.

Experimental results agree well with the prediction from the numerical wave tank. This means that for these monochromatic inhomogeneous waves of low steepness, the numerical model manages to predict accurately how waves propagate in the physical basin. It
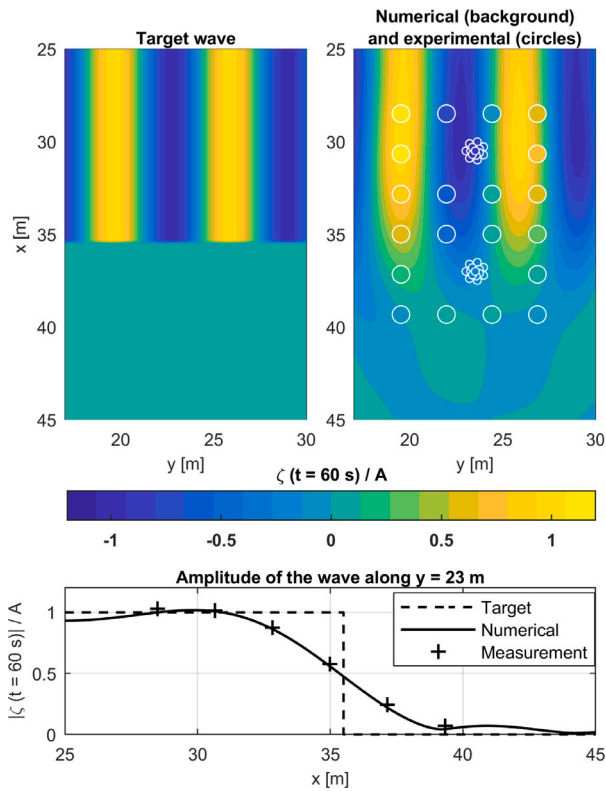
Fig. 5. Comparison of the free-surface elevation of the target wave, the numerical results and the experimental measurements (each circle represents one wave probe), for the synthetic target wave at $T = 2$ s, before reflection from the beach — Snapshot of free-surface elevation, and evolution of the amplitude of the waves along the transverse direction.
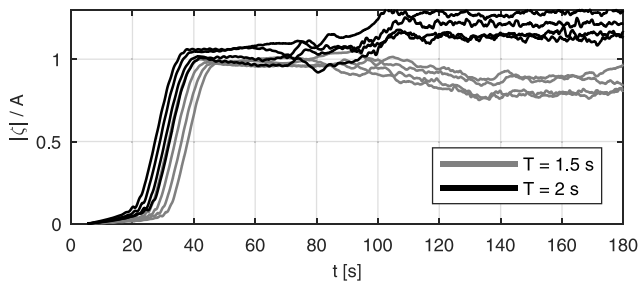

Fig. 6. Time series of the amplitude of the free-surface elevation for the 4 wave probes at $x = 28.5$ m, and for both wave periods.

also shows that the comparison should always be made in two steps: comparing the target wave to the results from the numerical wave tank, to check if the target wave is feasible in the basin, or at least how close one can hope to get. Then, comparing the numerical results to the experimental measurements, to see whether unexpected discrepancies appear between the numerical model and the experiments.

4.3. Reflection

Time series of the amplitude of the free-surface elevation for the three minutes of the experiment are presented for both wave periods in Fig. 6. The amplitudes were obtained with a Hilbert transform. Several stages appear. First, for approximately the first 20 s, waves are propagating from the wavemaker, but have not yet reached the wave probes. Then, a ramp in time, also present in the control signal of the wavemaker, lasts 20 s. The amplitude reaches then a constant

value until the reflection from the beach reaches the probes, at approximately $t = 80$ s. This confirms the choice of time window defined in Section 3.2.2.

5. Case study: Waves in sulafjorden

In order to test the method for a more realistic test case, it was tested for two sites in Sulafjorden, in one and the same sea state. The target wave was obtained by simulating the wave propagation in a fjord with a fully nonlinear potential flow numerical solver. Then, the optimization process was conducted as for the synthetic wave.

5.1. Test cases

5.1.1. Domains

The two sites correspond to two different positions that were considered for crossing Sulafjorden as part of the E39 project (Statens Vegvesen, 2022). The first one (corridor K1) is at the entrance of the fjord, while the second one (corridor K2) is located further inside the fjord (see Fig. 7). Swell waves can propagate without meeting obstacles from offshore to most of the domain for the first site, while some of it is hidden by the coast. This is a specificity of this location, as waves in fjord are often dominated by wind waves. For the second site, waves need to be diffracted or reflected in order to reach the domain, and a more complex wave field is expected. As often, this fjord is deep and sheltered. Except on the sides of the first domain, for all wave periods considered, deep water can be assumed, with errors on the dispersion relationship of less than 1%.

Pitch-roll buoys have been installed at the entrance of the fjord (buoy D in Fig. 7), as well as in both domains: buoy A in the first domain, and buoy C in the second domain. Data from the buoys is publicly available (Furevik et al., 2020), and scatter diagrams for the waves at each buoy are presented in Fig. 8. The effect of sheltering can be clearly seen, since the range of values for H_s decreases when the buoys go further away from the sea. For the second domain (buoy C), most of the historical sea states are well within the limits of application of linear wave theory. For the first domain (buoy A), some of the historical sea states are above the limit given by Le Méhauté (1969). However, this limit is arbitrary, and, as the steepness always remains close to the domain of applicability of linear wave theory, a good fit with predictions from linear wave theory can still be expected. Of course, this does not apply to non-sheltered zones outside the fjord. Thus, a nonlinear solver is needed to obtain the target wave by simulating wave propagation from an offshore location.

5.1.2. Sea states

The chosen sea state is that of a storm, that happened on January 1st, 2019. According to measurements from the most exposed buoy to the open sea (buoy D in Fig. 7), the significant wave height reached $H_s = 8$ m and the peak wave period around $T_p = 16$ s during the storm. Waves propagated mainly from the North West. This case is a good representation of the 100-year extreme conditions in the area according to the analysis by Furevik and Aarnes (2021).

5.1.3. Simulation of wave propagation in the fjord

The method presented in Section 2 requires a target wave defined by time series of free-surface elevation $\zeta(x, y, t)$ on an array of points across the domain of interest. As previously stated, unlike with homogeneous waves, the target wave field cannot be simply derived from a directional spectrum. Sea measurements of free-surface elevation can be directly obtained from buoys (Furevik et al., 2020), remote sensing with stereo video (Benetazzo et al., 2012) or LIDAR cameras (Desmars, 2020). However, such data does not always exist, and is often sparse (for buoys), or not covering large enough areas (less than 100×100 m in Benetazzo et al. (2012)). It was thus chosen to simulate wave
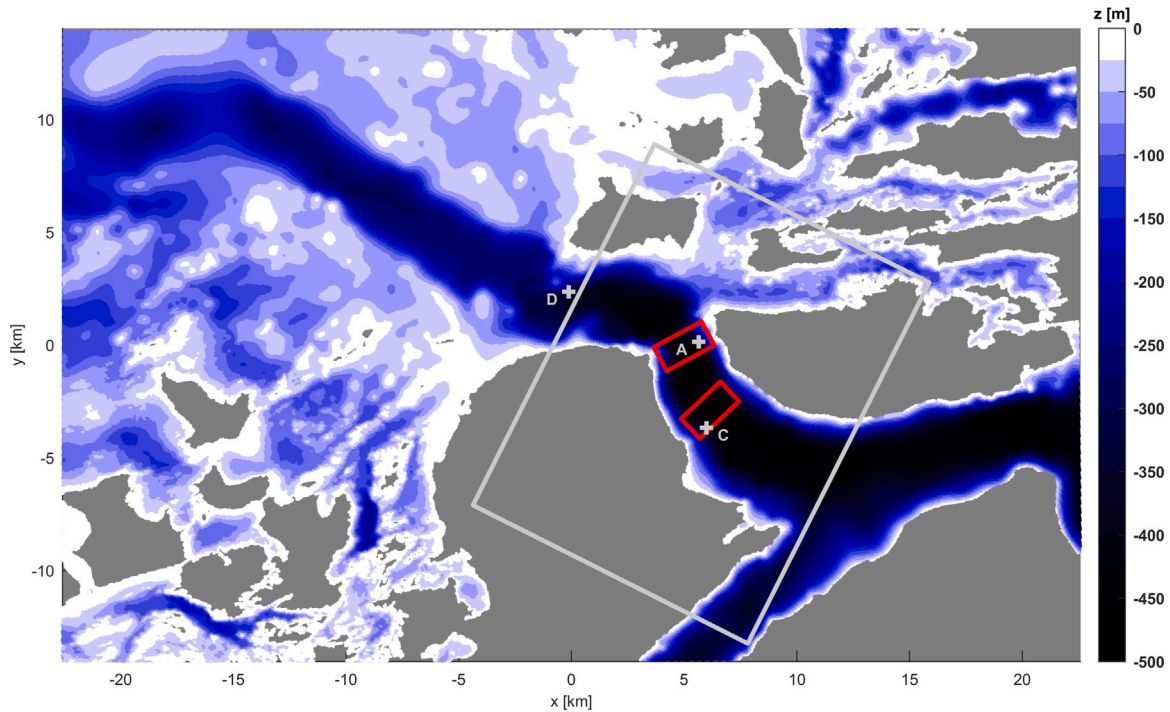
Fig. 7. Bathymetry of the region of Sulafjorden, with the location of the two domains indicated as red rectangles (domain 1 close to the fjord inlet and domain 2 inside the fjord), the location of the buoys indicated as grey crosses, and the computational domain used for the fully nonlinear potential flow numerical solver indicated by a grey rectangle.
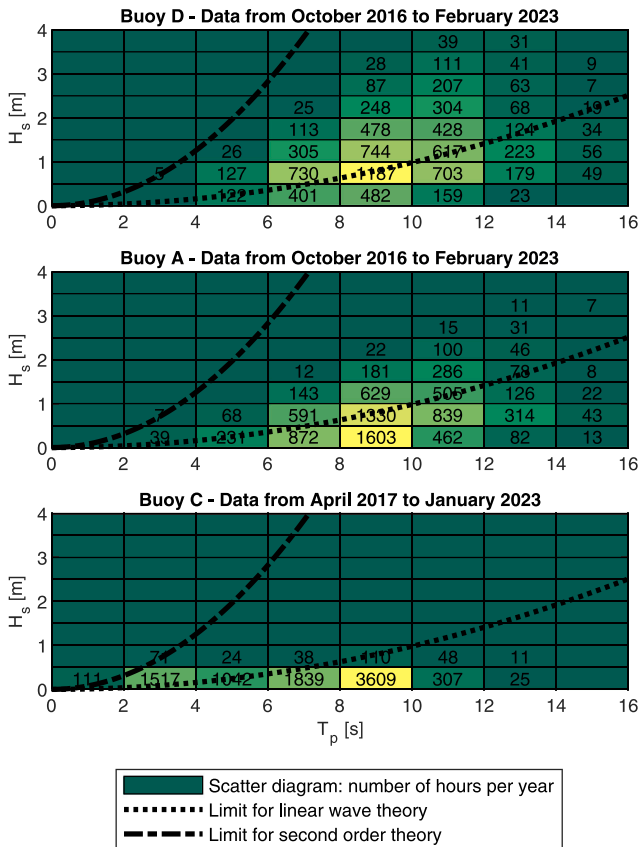

Fig. 8. Scatter diagrams from buoys in Sulafjorden, and limits for linear and second-order theory for regular waves in deep water, from Le Méhauté (1969) (respectively $H_s/(gT_p^2) = 0.001$ and 0.008).

propagation in the fjord with a numerical solver. As the phase of the target wave matters, a phase-resolving model had to be used.

Phase-resolving models such as the non-hydrostatic shallow water model SWASH (Zijlema et al., 2011), the high order spectral model HOS-ocean (Ducrozet et al., 2016), or the fully nonlinear potential flow model REEF3D::FNPF Bihs et al. (2020), are used in ocean and coastal engineering to realistically simulate the propagation of ocean waves. The choice of the appropriate model mainly depends on the area of interest, e.g., deep or shallow water area.

The fully nonlinear potential flow numerical solver REEF3D::FNPF is a phase-resolving model that has been developed by NTNU (see Bihs et al., 2020). Wang et al. (2022) investigated its capabilities in modelling accurately and efficiently free-surface waves in complex coastal areas such as those of the Norwegian coast (with rapid bathymetry variations and highly irregular coastline, with fjords and a large number of isles). This was then done more precisely for the case of Sulafjorden in Wang et al. (2023).

It is thus this model that was used to obtain waves representing realistic conditions for the two domains in Sulafjorden and that were chosen as target waves. The method is the one from Wang et al. (2023) but with the computational domain presented in Fig. 7, and a cell size of $dx = 20$ m (full scale).

The offshore waves propagate in Sulafjorden (wave buoys A and C) through Breisundet (wave buoy D), a channel directly exposed to the open sea. This is why, as in Wang et al. (2023), a prescribed wave was used as boundary condition for the North West boundary, while a radiation condition was enforced for all other boundaries. The North West boundary condition was calculated using a JONSWAP spectrum based on the storm case observed on January 1st, 2019, and long-crested waves. The simulation encompasses the 3-hour wave conditions during the peak of the storm. The irregular bathymetry was obtained from open-access high-resolution data from the Norwegian mapping authority (Kartverket Sjødivisjon, 2015). Again, the purpose here is to obtain a complex inhomogeneous wave field with a realistic background to test the flap motion optimization method, rather than to simulate storm waves in Sulafjorden with the best accuracy.
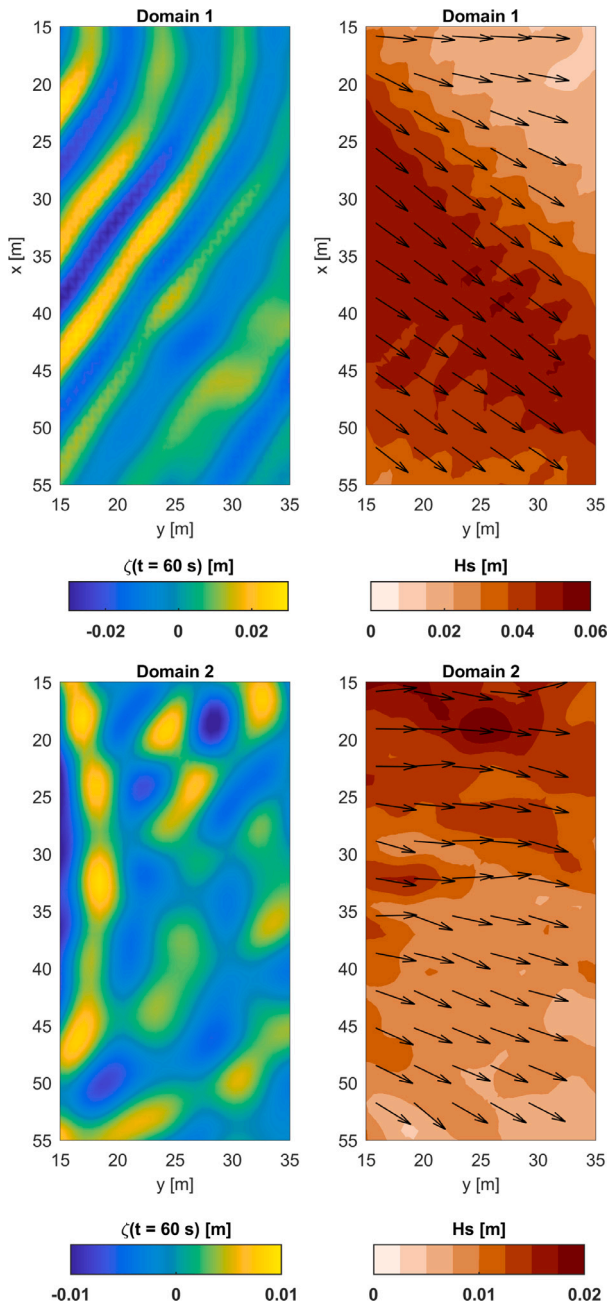
Fig. 10. Directional spectra obtained through Fourier Transform for two locations in each of the two domains, at $y = 25$ m – Data from the target wave – Each radial line represents 0.2 Hz — Model scale.

As previously mentioned, upon propagation in the fjord, energy is lost, and the significant wave height decreases. In addition to this effect, because of interactions with the bathymetry and the coast, waves become more short-crested and inhomogeneous. The first domain, at the entrance of Sulafjorden, still presents a relatively simple wave field. There is one dominant wave direction for swell, with nonetheless some shadowing effect from the coast. For the second domain however, waves have propagated inside the fjord, and the wave field becomes more complex: the spectrum of the swell presents two peaks at distinct directions, that are also dependent on the position in the domain (see Fig. 10).

5.1.5. Feasibility of the target wave in an ideal basin

For the case of the synthetic wave in Section 4, the target wave was not a solution of the 2D Helmholtz equation. In other words, the target wave was not feasible, even with a perfect control of the boundary conditions of the domain. For that reason, large discrepancies between the target wave and the numerical wave tank could be observed in the region around the step. Before conducting experiments, it is thus important to check whether the target wave is feasible, in order to be able to categorize the sources of differences between the target wave and the experiments in the Ocean basin.

The goal here is to assess how close the target wave is to a wave that could be generated in an ideal basin, within the assumptions of linear wave theory and constant water depth. By ideal basin, what is meant is a basin for which there is perfect control over all boundary conditions (and of constant water depth). In such a basin, it is possible to reproduce any solution for propagating waves, within those same assumptions.

In order to model this ideal basin, the same numerical wave tank and optimization method were used as for the physical basin. The only difference is in the boundary conditions. The ideal basin is a rectangular basin, for which all sides are wavemakers. The wavemakers are considered transparent to incoming waves, in order to have perfect active absorption, and the width of each individual flap is a third of

Fig. 9. Snapshot of ζ at $t = 60$ s and map of H_s and local wave direction for the target wave in each domain – Model scale – Different colour scales are used for each domain.

5.1.4. Description of the target waves

Fig. 9 presents a snapshot of the free-surface elevation for the target wave in each domain, and a map of the significant wave height and local wave direction. The local wave direction is defined as the average in time of the direction following the gradient of the free-surface elevation. Fig. 10 presents local directional spectra at two different locations in each of the two domains. The results are given in model scale, $1:60$. The spectra were obtained using directly a 3D Fourier transform, with a Gaussian window in space, and with the data from the target wave. Looking at the wave direction can be misleading in the case of a directional distribution with several peaks. Indeed, for the second domain, it can be seen from both the snapshot and the directional spectrum at $x = 20$ m that several wave systems with different directions are interacting. But this cannot be seen with a map of H_s and local wave direction.
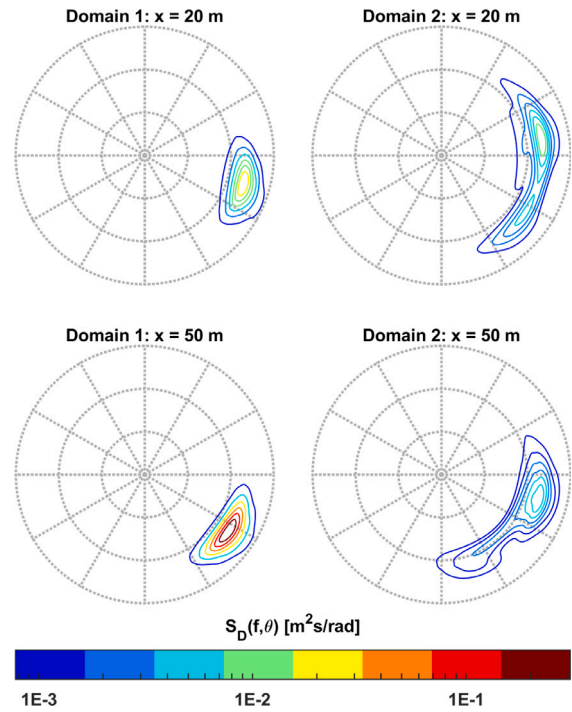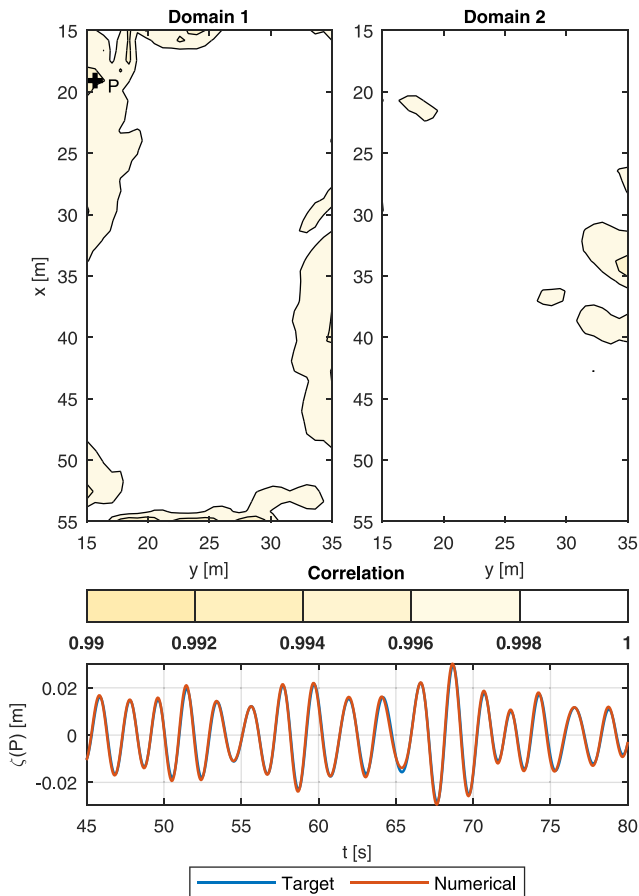
Fig. 11. Comparison of the target wave to a solution obtained from linear wave theory, using optimization in the ideal basin, and for both domains — Time series compared for domain 1 at the point P (placed at the position with lowest correlation).

the wavelength, which is less than the maximum width required by the Nyquist–Shannon criterion. As the flaps have a finite width, there are evanescent modes because of aliasing (Schäffer, 1998). There is thus a need for a margin, that is a minimum distance, between the wavemakers and the area of interest, so that the evanescent modes have decayed. Let the criterion be that all evanescent modes should have decayed more than 95% in amplitude. With a scale of $1 : 60$ and a margin of 10 m in model scale, the criterion is met for all wave periods $T < 34$ s in full scale (see Eq. (7) in Appendix). For linear components of ocean waves, this is more than enough. The margin has thus been set to 10 m for the ideal basin.

The optimization method described in Section 2.3 is then used to generate the closest feasible solution to the target wave in this ideal basin. The process is done for the realistic fjord wave, for both domains, with the target wave obtained from the fully nonlinear potential flow model. A map of the correlation coefficient of the free-surface elevation across the entire area is presented in Fig. 11, for both domains. In both cases, the correlation exceeds 99.4% everywhere in the area. This does not prove that the target wave accurately represents waves found in Sulafjorden. However, it shows that contrarily to the synthetic wave in Section 4, both target waves here are close to feasible waves. It also shows that the assumptions of linear wave theory and constant water depth were reasonable.

Indeed, in a physical basin, sources of differences between the target wave and experimental measurements can be divided into four categories:

- Non-physical target wave (as for the synthetic wave in Section 4)

- Discrepancies due to the assumptions of linear wave theory and constant water depth
- Theoretical limits of the basin (it is not possible to perfectly prescribe all boundary conditions in an experimental facility)
- Discrepancies between the numerical wave tank and the experiments

Of those, the study of the feasibility of the target wave has shown that the first two could explain only up to 0.6% of any loss in correlation. The third category is then the reason for any higher loss of correlation between the target wave and the numerical wave tank, while the fourth is the sole reason for differences between the numerical wave tank and the experiments.

5.2. Results

The optimization method described in Section 2.3 was applied to both target waves. This gave the control signal to send to each flap of the wavemaker (BM3 in Fig. 1). The numerical wave tank also gave a prediction of the time series of free-surface elevation across the domain. Experiments were then conducted in SINTEF's Ocean basin, with each wave being repeated for 6 different positions of the wave probes array.

5.2.1. First domain
Results from the Ocean basin tests for the first domain are provided in Fig. 12. Those results provide a comparison of the free-surface elevation from the target wave, the numerical wave tank, and the experimental measurements. Time series of measured free-surface elevation from those three sources are compared for two points, P1 and P2, whose positions are indicated by black crosses in the figure. The time series match well, with the largest discrepancies being observed between the target wave and the numerical results. This means both that the target wave can be well reproduced in this Ocean basin, and that the propagation of waves in the physical basin is well captured numerically.

Two graphs of correlation coefficients between time series of free-surface elevation, ζ, are also presented; one with the correlation between the target wave and the numerical results at each point of the domain, and another one with the correlation between the numerical results and the experimental data, for each one of the wave probes. In most of the basins, and for the two comparisons, the correlation coefficient is higher than 0.98, indicating that the time series match overall — the difference that can be observed at P2 between the time series for the target and the numerical waves still leads to a correlation coefficient above 0.98. Some loss of correlation can be observed in the top right corner of the basin. This is especially the case between the target wave and the numerical results, which is consistent with the observations made on the time series. There are at least two possible explanations for those observations. The first one is that this corner corresponds to an area with waves of lesser amplitude (see Fig. 9), which means that a constant noise across the basin would lead to a higher loss of correlation in this corner. The other one is that, as the multiflap wavemaker is on the left side (at $y = 0$ m), with this Ocean basin, it is more difficult to reproduce a component travelling downwards (along increasing x) there than anywhere else in the basin.

5.2.2. Second domain
Results from the Ocean basin tests for the second domain are provided in Fig. 13. As for the first domain, the figure offers a comparison of the free-surface elevation from the three different datasets (target wave, numerical, and experimental results), and the interpretation of possible observed differences still holds.

Even though the time series at both points still match quite well, the differences are higher than for the first domain. The discrepancies between the numerical predictions and the experimental measurements show no clear pattern in space across the domain, with correlations
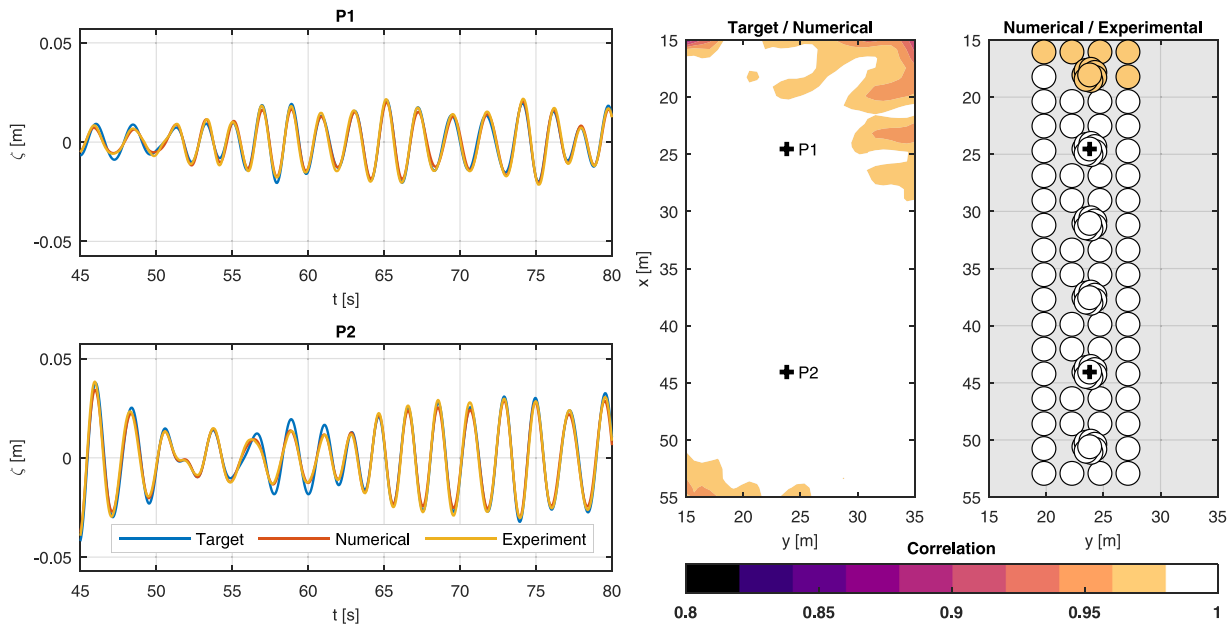
Fig. 12. Comparison of experimental, numerical and target waves time-series for the first domain and before reflection from the beach, in terms of time-series at two points, and of correlation on the whole domain of the free-surface elevation between $t = 45$ s and $t = 80$ s – Domain 1 – For the experimental data, each circle corresponds to one wave probe.

Fig. 13. Comparison of experimental, numerical and target waves time-series for the second domain and before reflection from the beach, in terms of time-series at two points, and of correlation on the whole domain of the free-surface elevation between $t = 45$ s and $t = 80$ s – Domain 2 – For the experimental data, each circle corresponds to one wave probe.
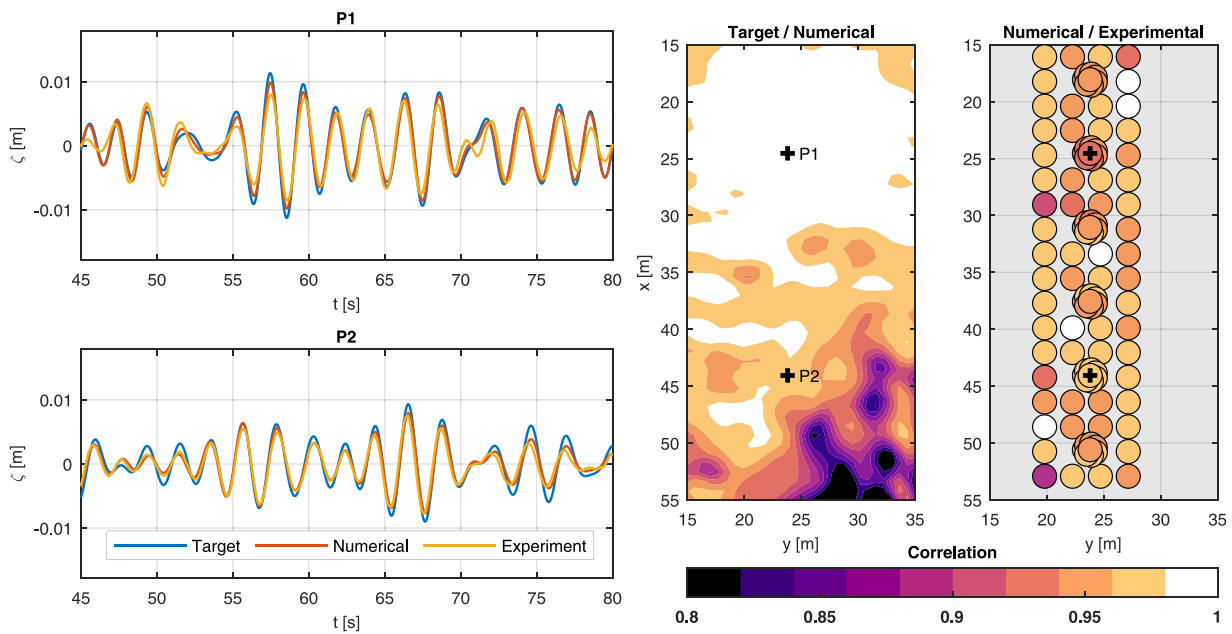
everywhere ranging between 0.93 and 0.99, except for two probes at the corners of the domain. This trend was expected as, compared to the first domain, waves in this case have lower amplitudes (which means that a constant noise leads to a higher loss of correlation). The wave system for the second domain is also more complex, with larger inhomogeneities and directional spreading. It is unsure whether this factor also contributes to the loss of correlation.

The differences between the target wave and the numerical results show a clear pattern: the correlation is high in the upper half of the domain, but drops in the lowest half. Close to the boundary of the domain at $x = 55$ m, the wave system has a large directional spreading (as can be seen in the directional spectrum shown in Fig. 10 for $x = 50$ m). Although the target waves travel mostly downwards (in

the positive x-direction), there are also components travelling upwards entering the domain at this boundary. As was indicated when discussing results for the first domain, since there is only one multiflap wavemaker, at $y = 0$ m, and since this wavemaker is limited in width, these components cannot be accurately reproduced experimentally in this basin, and this limitation is well captured by the numerical wave tank. This shadowing effect, described in Gilbert and Huntington (1991), will be further discussed in Section 5.2.3.

5.2.3. Limitations of the basin

As previously stated, differences between the target wave and results from the numerical wave tank indicate limitations of the physical basin. Thus, for the second domain, an explanation for the loss of
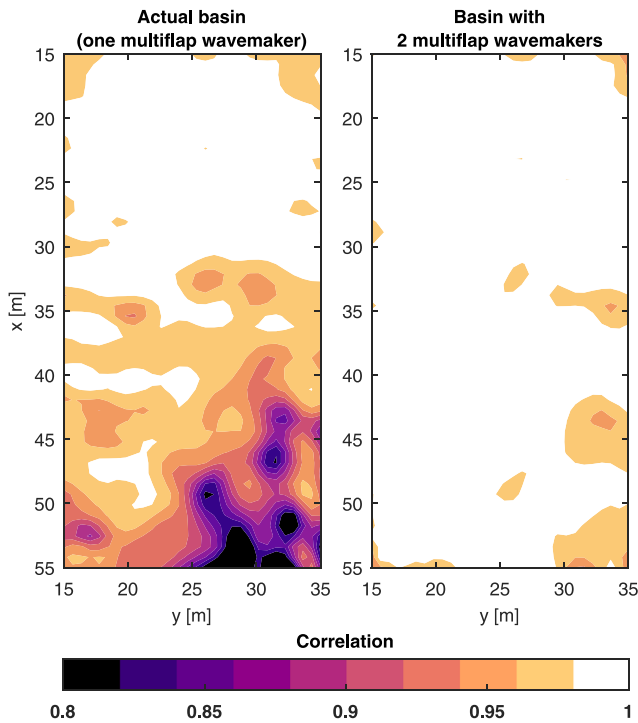
Fig. 14. Correlation between the free-surface elevation of the target wave and the numerical results from the optimization, for the second domain, between $t = 45$ s and $t = 80$ s, and for two basins. The first one being the actual basin described in Section 3.1, and the second one being a basin with two multiflap wavemakers, covering the sides of the basin at $x = 0$ m (left) and at $y = 62$ m (bottom).

correlation on the lower half of the basin in Fig. 13 can be that there is only one multiflap wavemaker, and a beach instead of a wavemaker on the bottom side, for $x > 62$ m. In order to verify this assumption, the optimization process is performed again, but for a different basin geometry, namely a basin with still a multiflap wavemaker at $y = 0$ m, but also an additional multiflap wavemaker on the bottom side, at $x = 62$ m. Results for the correlation coefficients between the target wave and the predictions from the numerical model are shown in Fig. 14, for both numerical basin geometries. As expected, there is a large improvement in wave quality in the lower half of the basin, with correlation coefficients reaching that of the upper half, and everywhere above 0.95. This confirms that the low wave quality can be explained by a shadowing effect.

5.2.4. Correction of error in probes position

Except for the central circular array (see Fig. 2), the other probes were mounted on the metallic frame for the purpose of this experimental campaign only. The wave probes were mounted in two steps. First, a metallic frame was installed on the moving carriage. Then, the waves probes were mounted on the frame. The displacements of the carriage between tests were measured automatically, with great precision ($\approx$ 1 cm). The positions of the probes were measured by the authors with measuring tape, with much larger uncertainties. This was done in two steps. First, the authors measured the positions of the probes relative to each other. Then was measured the position of one probe $\mathbf{X}_1$ and of the frame relative to the coordinate system of the basin. The position of each probes is thus a sum of two terms, $\mathbf{X}_i = (\mathbf{X}_i - \mathbf{X}_1) + \mathbf{X}_1$, and the error in their position can be written as $\Delta \mathbf{X}_i = \epsilon_i + \epsilon_0$, where ϵ_0 is the average error for all probes. Neglecting errors in the measurement of the displacements, $\Delta \mathbf{X}_i$ is a bias that is constant across all tests.

Assuming homogeneity locally, with a given directional spectrum $E(\omega, \theta)$ – following the notations of Barstow et al. (2005) – the correlation between two times series $\zeta_1(t)$ and $\zeta_2(t)$ recorded at two points

distant of $\Delta \mathbf{X} = \mathbf{X}_2 - \mathbf{X}_1$ is:

$$\rho_{\zeta_1, \zeta_2} = \frac{1}{\iint E} \iint_{\omega, \theta} \cos\left(\mathbf{k}(\omega, \theta) \cdot \Delta \mathbf{X}\right) E(\omega, \theta)\, d\theta d\omega \qquad (6)$$

For the directional spectra of both domains presented in Fig. 10, the correlation can already drop to as low as 0.91 for $\|\Delta \mathbf{X}\| = 0.5$ m.

Thus, the existence of a bias in the probes position was investigated. Numerically, time series of free-surface elevation can be obtained for any point. The position of the probes is then shifted in space, and the correlation coefficient between the numerical wave tank and the experimental data is calculated as a function of this shift. An optimal shift can thus be defined for each probe and each test, as the one for which the correlation coefficient reaches a maximum. If this optimal shift is constant across all tests, and all probes, then we can assume that this shift is equal to ϵ_0, and correct for it. In doing so, there is a risk of artificially improving the quality of the results (if the optimal shift is not equal to $\Delta \mathbf{X}_i$). As the estimation of an average bias ϵ_0 is statistically more significant than that of each ϵ_i separately, in order to not artificially improve the quality of the results, the correction was only done for ϵ_0.

For the synthetic wave (Section 4), only the optimal shift in the x direction was estimated (as the wave is mostly long-crested). It was done directly from the evolution of the wave amplitude along a transverse line (see Figs. 4 and 5). The shifts are respectively of $\Delta x = -0.3$ m for $T = 1.5$ s, and of $\Delta x = -0.35$ m for $T = 2$ s.

For the fjord waves, both presented a clear bias across all tests (for each domain, 6 tests were run, to have the frame at 6 different positions). The bias observed in x- and y-directions were respectively of -0.35 m and -0.35 m for the first domain, and of -0.35 m and -0.4 m for the second domain. A constant spatial bias appears across all test cases. In all the results and figures that appear in the present article, all probes coordinates were thus shifted by a constant vector $\Delta \mathbf{X} = (-0.35, -0.375)^T$ m.

5.3. Discussion and next steps

Even though for both test cases, measured waves in the basin match overall well with the numerical predictions, the method presented in the present article is not without shortcomings. First, the model did not take into account reflections from the beach facing the wavemaker, and the measurements were accordingly taken before reflection. When looking at wave statistics, long time series are needed, and reflection has to be taken into account when looking at wave quality. This issue is, however, not specific to inhomogeneous waves.

Fjords are a specific category of coastal areas, that are partly sheltered, narrow and deep channels. The combination of the complex geometry, the local wind conditions and the incoming offshore waves often create an inhomogeneous wave field in the fjords. However, inhomogeneous waves can also be observed in coastal areas with direct exposure to open sea. Therefore, the method should be tested and maybe expanded for steeper sea states. Likewise, typical coastal areas can have intermediate or shallow water. The main question would then be whether it is possible to reproduce inhomogeneous waves with a high quality in a basin of constant water depth, when bathymetry varies with a scale similar to that of the structure.

Two other remaining challenges should also be pointed out. It is still being determined which target waves are needed to test large floating structures. The present article focuses on the experimental reproduction of a given wave field, and special care was given to reproduce a sufficiently realistic target wave, so that the results would be relevant for actual model tests. Simulating the propagation of waves from an offshore spectrum with a phase-resolving solver for each realization is time-consuming. It would therefore be interesting to investigate alternative methods to treat wave statistics in inhomogeneous wave fields. This is especially the case if wind waves are dominant compared to swell. Even though the fjord chosen in the case study is a fjord

exposed to swell, in the context of the Norwegian coastal highway route E39 project, other fjords are dominated by wind waves.

Lastly, it should be noted that one of the most important aspects of model tests is the control of wave conditions, that is, knowing which waves are present in the basin. When generating complex wave fields, data post-processing also becomes more intricate. This increased complexity can lead to challenges in comprehending the outcomes of the model test and explaining any observed disparities.

6. Conclusions

A method to reproduce an inhomogeneous wave field in an Ocean basin has been presented. The method has been tested for a case corresponding to arbitrary target waves, and two cases corresponding to realistic fjord waves. In all cases, linear wave theory is applicable over at least a few wavelengths, and deep water can be assumed. Overall, before reflection from the beach, the measured waves in the basin match well with both the target wave and the numerical predictions. For a simple case, short-crested waves with one dominant direction, correlations are above 0.98, except at the corners of the domain. For a more complex case, with a large directional spreading and a complex pattern of inhomogeneities, two phenomena are observed. The discrepancies between the numerical model and the experiments increase, with correlations down to 0.93. However, this could also be explained by the very low amplitude of the waves. Shadowing effects from the beach on the side of the wavemaker also appear, reducing the available working area. Having multiflap wavemakers on two sides of the basin instead of only one helps greatly enlarging the working area.

CRediT authorship contribution statement

Sébastien Laflèche: Conceptualization, Methodology, Software, Validation, Formal analysis, Investigation, Writing – original draft. **Konstantinos Christakos:** Resources, Writing – original draft. **Babak Ommani:** Conceptualization, Supervision, Writing – review & editing. **Sébastien Fouques:** Conceptualization, Writing – review & editing. **Trygve Kristiansen:** Conceptualization, Writing – review & editing.

Declaration of competing interest

The authors declare that they have no known competing financial interests or personal relationships that could have appeared to influence the work reported in this paper.

Data availability

Upon request, the authors will evaluate sharing the data together with other parties sharing the data ownership.

Acknowledgement

Appendix. Minimum required flap width

A multiflap wavemaker consists of individual panels (flaps in the present Ocean basin) of finite width. Too large flaps can result in spurious waves, that can be either propagating or evanescent (Biésel, 1954). Let us consider an infinitely wide wavemaker at $x = 0$ m, with discrete panels of width l_p. Let us consider the generation of an oblique wave of wavenumber k_0, at an angle θ from the normal to the wavemaker. Its wavenumber in the y-direction is $k_0^y = k_0 \sin(\theta)$.

If a wave profile has a wavenumber in the y-direction k_y, then the wavenumber in the x-direction is k_x, so that $k_0^2 = k_x^2 + k_y^2$. If $|k_y| > k_0$,

then k_x is imaginary, and the mode is evanescent. The rate at which it decays is $\exp(-\kappa x)$, where $\kappa = \sqrt{k_y^2 - k_0^2}$.

As the width of the panels is finite, the displacement of the wavemaker is a piecewise constant function of y. This creates aliasing, so that modes in $k_y = k_0^y + n k_p$ appears, where $k_p = 2\pi / l_p$ and $n \in \mathbb{Z}$. The non-trivial criterion to avoid the generation of spurious propagating waves is then $|\sin(\theta)| < k_p / k_0 - 1$, as is also given by Gilbert and Huntington (1991). The practical criterion given by Biésel (1954) and recommended by ITTC (2017), includes an additional margin: $|\sin(\theta)| < k_p / k_0 - \sqrt{2}$. This margin ensures that evanescent modes have also decayed.

Indeed, if for a given n, $|k_0^y + n k_p|$ is close to k_0, then the associated component will be evanescent, but slowly decaying. The goal then is to ensure that all evanescent modes have decayed before entering the area of interest for the experiments. Let L be a margin: the distance between the wavemaker and the working area. If what is considered acceptable is that all evanescent modes have lost at least 95% of their amplitude when entering the working area. Then the condition will read: $\exp(-\kappa L) < 0.05$. If this condition is to be met for all n and for all values of θ, then the resulting limitation is:

$$\frac{\lambda}{l_p} > 1 + \sqrt{1 + \left(\frac{3}{k_0 L}\right)^2} \tag{7}$$

If the margin is set as $L = 3/k_0 \approx \lambda/2$, then the criterion becomes that from Biésel (1954).

References

Abrahamsen, B.C., Stansberg, C.T., 2019. LFCS Review report – Model testing of large structures in a wave basin. Research report OC2018 A-073 - WP5, SINTEF Ocean, p. 36.

Barstow, S.F., Bidlot, J.-R., Caires, S., Donelan, M.A., Drennan, W.M., Dupuis, H., Graber, H.C., Green, J.J., Gronlie, O., Guérin, C., 2005. Measuring and analysing the directional spectra of ocean waves. In: COST Action, (714), Office for Official Publications of the European Communities, Luxembourg.

Benetazzo, A., Fedele, F., Gallego, G., Shih, P.-C., Yezzi, A., 2012. Offshore stereo measurements of gravity waves. Coast. Eng. 64, http://dx.doi.org/10.1016/j.coastaleng.2012.01.007.

Biésel, F., 1954. Wave machines. In: Proceedings of the First Conference on Ships and Waves. Hoboken, New Jersey, pp. 288–304.

Biésel, F., Suquet, F., 1951. Les Appareils générateurs de houle en laboratoire. Houille Blanche (2), http://dx.doi.org/10.1051/lhb/1951033.

Bihs, H., Wang, W., Pakozdi, C., Kamath, A., 2020. REEF3D::FNPF—A flexible fully nonlinear potential flow solver. J. Offshore Mech. Arct. Eng. 142 (4), http://dx.doi.org/10.1115/1.4045915.

Cheng, Z., Gao, Z., Moan, T., 2018. Wave load effect analysis of a floating bridge in a fjord considering inhomogeneous wave conditions. Eng. Struct. 163, http://dx.doi.org/10.1016/j.engstruct.2018.02.066.

Cheng, Z., Svangstu, E., Gao, Z., Moan, T., 2019. Field measurements of inhomogeneous wave conditions in bjørnafjorden. J. Waterw. Port Coast. Ocean Eng. 145 (1), http://dx.doi.org/10.1061/(ASCE)WW.1943-5460.0000481.

Christakos, K., Gao, Z., Furevik, B.R., Björkqvist, J.-V., Aarnes, O.J., 2022. In situ coastal observations of wave homogeneity and coherence. Appl. Ocean Res. 129, http://dx.doi.org/10.1016/j.apor.2022.103390.

Dai, J., Leira, B.J., Moan, T., Alsos, H.S., 2021. Effect of wave inhomogeneity on fatigue damage of mooring lines of a side-anchored floating bridge. Ocean Eng. 219, http://dx.doi.org/10.1016/j.oceaneng.2020.108304.

Dalrymple, R.A., 1989. Directional wavemaker theory with sidewall reflection. J. Hydraul. Res. 27 (1), http://dx.doi.org/10.1080/00221688909499241.

Desmars, N., 2020. Real-time reconstruction and prediction of ocean wave fields from remote optical measurements (Ph.D. thesis). École centrale de Nantes.

Ducrozet, G., Bonnefoy, F., Le Touzé, D., Ferrant, P., 2016. HOS-ocean: Open-source solver for nonlinear waves in open ocean based on High-Order Spectral method. Comput. Phys. Comm. 203, 245–254. http://dx.doi.org/10.1016/j.cpc.2016.02.017.

Dunham, K.K., 2016. Coastal Highway Route E39 - Extreme Crossings. In: Transportation Research Procedia, vol. 14, Elsevier B.V., pp. 494–498. http://dx.doi.org/10.1016/j.trpro.2016.05.102.

Furevik, B.R., Aarnes, O.J., 2021. Wave conditions in Sulafjorden, Vartdalsfjorden, Valsafjorden and Julsundet. METreport No. 3/2021, Norwegian Meteorological Institute, pp. 17–18.

Furevik, B.R., Lønseth, L., Borg, A.L., Neshaug, V., Gausen, M., 2020. Oceanographic observations for the Coastal Highway E39 project in Mid-Norway. http://dx.doi.org/10.21343/ef2d-jp97.

Gilbert, G., Huntington, S.W., 1991. A technique for the generation of short crested waves in wave basins. J. Hydraul. Res. 29 (6), http://dx.doi.org/10.1080/00221689109498959.

ITTC, 2017. Laboratory Modelling of Multidirectional Irregular Wave Spectra. Recommended Procedures and Guideline 7.5-02-07-01.1, Specialist Committee on Modelling Environmental Conditions of 28th ITTC.

Kartverket Sjødivisjon, 2015. Produktark: Sjøterrengmodeller. Kartverket (Norwegian Mapping and Cadastre Authority).

Laflèche, S., Ommani, B., Kristiansen, T., Fouques, S., 2023. Wave inhomogeneities in a wave basin of constant water depth. Ocean Eng. 283, http://dx.doi.org/10.1016/j.oceaneng.2023.115007.

Le Méhauté, B., 1969. An Introduction To Hydrodynamics and Water Waves, Vol. 2: Water Wave Theories. ESSA Technical Report, Pacific Oceanographic Laboratories., U.S. Department of Commerce, Environmental Science Services Administration.

MATLAB, 2022. version 9.12.0 (R2022a). The MathWorks Inc., Natick, Massachusetts.

Matsumoto, A., Hanzawa, M., 1996. New optimization method for paddle motion of multi-directional wavemaker. In: Coastal Engineering. American Society of Civil Engineers, Orlando, Florida, United States, http://dx.doi.org/10.1061/9780784402429.038.

Molin, B., 1991. Génération de Houle Multidirectionnelle dans un Bassin Rectangulaire, Application à une Petite Cuve à Houle. Technical Report No. 1.04.32.0390, DGA.

Ota, D., Houtani, H., Sawada, H., Taguchi, H., 2021. Optimization of segmented wavemaker control to generate spatially uniform regular waves in a rounded-rectangular wave basin. In: Ocean Engineering, vol. 6, American Society of Mechanical Engineers, Virtual, Online, http://dx.doi.org/10.1115/OMAE2021-62773.

Rodrigues, J.M., Viuff, T., Økland, O.D., 2022. Model tests of a hydroelastic truncated floating bridge. Appl. Ocean Res. 125, 103247. http://dx.doi.org/10.1016/j.apor.2022.103247.

Schäffer, H.A., 1996. Second-order wavemaker theory for irregular waves. Ocean Eng. 23 (1), http://dx.doi.org/10.1016/0029-8018(95)00013-B.

Schäffer, H.A., 1998. Some design aspects of an absorbing 3D wavemaker. In: Coastal Engineering. American Society of Civil Engineers, Copenhagen, Denmark, http://dx.doi.org/10.1061/9780784404119.080.

Schäffer, H., Steenberg, C., 2003. Second-order wavemaker theory for multidirectional waves. Ocean Eng. 30 (10), http://dx.doi.org/10.1016/S0029-8018(02)00100-2.

Statens Vegvesen, 2022. E39 Sulafjorden, fjordkryssing. URL https://www.vegvesen.no/vegprosjekter/europaveg/e39sulafjorden/. (Accessed 02 May 2024),

Stefanakos, C., Dai, J., Leira, B., 2021. Investigation of inhomogeneous wave conditions in Sulafjorden. In: The 31st International Ocean and Polar Engineering Conference. OnePetro, Rhodes, Greece.

Takayama, T., 1984. Theory of oblique waves generated by serpent-type wave-maker. Coastal Eng. Japan 27 (1), http://dx.doi.org/10.1080/05785634.1984.11924374.

Wang, W., Pákozdi, C., Kamath, A., Bihs, H., 2023. Fully nonlinear phase-resolved wave modelling in the Norwegian fjords for floating bridges along the E39 coastal highway. J. Ocean Eng. Mar. Energy http://dx.doi.org/10.1007/s40722-023-00284-z.

Wang, W., Pákozdi, C., Kamath, A., Fouques, S., Bihs, H., 2022. A flexible fully nonlinear potential flow model for wave propagation over the complex topography of the Norwegian coast. Appl. Ocean Res. 122, http://dx.doi.org/10.1016/j.apor.2022.103103.

Wei, W., Fu, S., Moan, T., Lu, Z., Deng, S., 2017. A discrete-modules-based frequency domain hydroelasticity method for floating structures in inhomogeneous sea conditions. J. Fluids Struct. 74, http://dx.doi.org/10.1016/j.jfluidstructs.2017.06.002.

Yang, P., Liu, X., Wang, Z., Zong, Z., Tian, C., Wu, Y., 2019. Hydroelastic responses of a 3-module VLFS in the waves influenced by complicated geographic environment. Ocean Eng. 184, http://dx.doi.org/10.1016/j.oceaneng.2019.05.020.

Zijlema, M., Stelling, G., Smit, P., 2011. SWASH: An operational public domain code for simulating wave fields and rapidly varied flows in coastal waters. Coast. Eng. 58 (10), http://dx.doi.org/10.1016/j.coastaleng.2011.05.015.